Experimental evidence consistent with a magnon Nernst effect in the antiferromagnetic insulator $MnPS_3$

Y. Shiomi,[1] R. Takashima,[2] and E. Saitoh[1,3,4,5]
[1]*Institute for Materials Research, Tohoku University, Sendai 980-8577, Japan*
[2]*Department of Physics, Kyoto University, Kyoto 606-8502, Japan*
[3]*WPI Advanced Institute for Materials Research, Tohoku University, Sendai 980-8577, Japan*
[4]*Advanced Science Research Center, Japan Atomic Energy Agency, Tokai 319-1195, Japan*
[5]*Center for Spintronics Research Network, Tohoku University, Sendai 980-8577, Japan*
(Received 12 June 2017; revised manuscript received 10 October 2017; published 25 October 2017)

A magnon Nernst effect, an antiferromagnetic analog of the magnon Hall effect in ferromagnetic insulators, has been studied experimentally for the layered antiferromagnetic insulator $MnPS_3$ in contact with two Pt strips. Thermoelectric voltage in the Pt strips grown on $MnPS_3$ single crystals exhibits nonmonotonic temperature dependence at low temperatures, which is unlikely to be explained by electronic origins in Pt but can be ascribed to the inverse spin Hall voltage induced by a magnon Nernst effect. Control of antiferromagnetic domains in the $MnPS_3$ crystal by magnetoelectric cooling is found to modulate the low-temperature thermoelectric voltage in Pt, which is evidence consistent with the emergence of the magnon Nernst effect in Pt-$MnPS_3$ hybrid structures.

DOI: 10.1103/PhysRevB.96.134425

I. INTRODUCTION

The Berry phase is a fundamental concept in solid-state physics and is responsible for a spectrum of physical phenomena [1]. One pronounced example caused by the Berry phase is the Hall effect of electrons. The Berry curvature of electrons manifests as the transverse velocity of the electrons, which gives rise to various Hall effects, e.g., anomalous Hall effects, topological Hall effects, and spin Hall effects [1–3]. In semiclassical theory, the Berry curvature can be regarded as an effective magnetic flux for conduction electrons, and the related effective Lorentz force bends the trajectory of moving electrons to the Hall direction [1–3].

Recently, the Berry phase concept has been expanded to magnon transport in ferromagnetic insulators [4,5]. In insulating magnets, the spin transport is governed by low-energy spin excitations, i.e., magnons. The ring-exchange process on ferromagnetic lattices leads to a Berry phase effect in magnon transport [4]. With certain types of lattice geometry and magnetic order, the net fictitious magnetic field due to the magnon Berry curvature survives, and there occurs the magnon Hall effect [4,5]. As shown in Fig. 1(a), the magnon Hall current produces a temperature gradient along the Hall direction, leading to finite thermal Hall conductivity. The magnon Hall effect has been demonstrated experimentally by the measurement of the thermal Hall effect (Righi-Leduc effect) for the pyrochlore ferromagnet $Lu_2V_2O_7$ [6] and other magnetic insulators [7–9].

In this paper, the topological magnon transport induced by the Berry curvature is experimentally expanded to antiferromagnetic insulators: the magnon-mediated spin Nernst effect, dubbed the magnon Nernst effect [10,11]. In a honeycomb antiferromagnet in the presence of the Dzyaloshinskii-Moriya (DM) interaction, a longitudinal temperature gradient can give rise to spin currents along the Hall direction, realizing a magnon Nernst effect [10,11]. This effect can be viewed as an antiferromagnetic analog of the magnon Hall effect in ferromagnetic insulators, which stems from a fictitious magnetic flux due to the magnon Berry curvature. As shown in Fig. 1(b), in a honeycomb antiferromagnet [10,11], both up-spin and down-spin magnons exhibit the magnon Hall effect under an applied in-plane temperature gradient, but magnons with opposite spins flow in opposite transverse directions. The thermal Hall current thereby cancels out, while a nonzero spin current emerges in the Hall direction. The generation of spin currents devoid of a thermal current without external magnetic fields should be a significant merit of antiferromagnetic spintronics [12].

As a material candidate to realize magnon Nernst effects, monolayer $MnPS_3$ has been theoretically discussed [10] and nonmonotonic temperature dependence of the magnon Nernst coefficient was predicted based on a low-temperature spin-wave approximation [see Fig. 4(d)]. Though growth of the monolayer $MnPS_3$ is experimentally challenging, a similar effect is expected in bulk $MnPS_3$ because of the two-dimensional crystal structure with tiny interlayer magnetic couplings [13]. Bulk single crystals of $MnPS_3$ have been intensively studied because of the two-dimensional character in the magnetic properties [14] and the easy intercalation of lithium and molecules [15]. In order to study the magnon Nernst effects expected in $MnPS_3$, we here prepare bulk single crystals of $MnPS_3$ and employ the technique of the inverse spin Hall effect [16] for electrical detection of the transverse spin current induced by the magnon Nernst effect. For Pt films grown on the edges of $MnPS_3$ single crystals, we have observed nonmonotonic temperature dependence of the thermoelectric voltage and also its dependence on antiferromagnetic domains of $MnPS_3$. These results indicate that the magnon Nernst effect induces inverse spin Hall voltage in the Pt-$MnPS_3$ structure.

II. EXPERIMENTAL METHOD

Bulk single crystals of $MnPS_3$ were grown by a chemical vapor transport method following a previous report [17]. Stoichiometric amounts totaling 5 g of elements Mn, P, and S were sealed into an evacuated quartz tube. The tube was placed in a horizontal three-zone furnace and heated slowly up

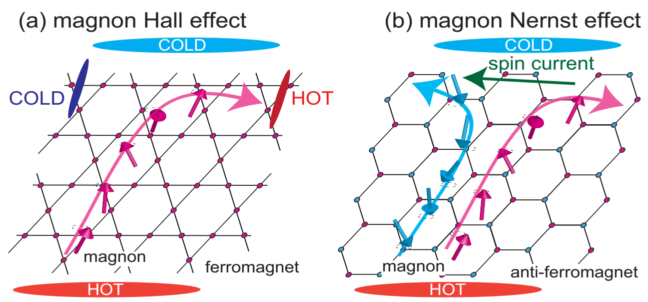

FIG. 1. Schematics of (a) the magnon Hall effect in kagome ferromagnets and (b) the magnon Nernst effect in honeycomb antiferromagnets.

to 630–680 °C; the temperature of the charge region was set at 680 °C and that of the growth region at 630 °C. A number of platelike single crystals of $MnPS_3$ were obtained in the growth region in 100 h. As shown in Fig. 2(a), the $MnPS_3$ single crystals are optically transparent with a green color. The largest surfaces of the crystals were determined by x-ray diffraction measurements to be the *ab* plane, as shown in Fig. 2(b). Manganese ions (Mn^{2+}) form a honeycomb lattice within the *ab* plane and the honeycomb lattices are stacked along the *c* direction with a weak van der Waals interlayer coupling [15].

The $MnPS_3$ single crystals are highly insulating below room temperature, which is suitable for studying spin-current generation free from magnetotransport effects inside $MnPS_3$. The magnetic property of $MnPS_3$ was studied using a superconducting quantum interference device (SQUID) magnetometer (Magnetic Property Measurement System, Quantum Design, Inc.). The temperature (T) dependence of the magnetization, M, for a $MnPS_3$ single crystal is shown in Fig. 2(c). Here, the external magnetic field (H) of 1 T was applied perpendicular to the crystal plane. With decreasing T from 300 K, M increases and shows a broad peak around 110 K, reflecting the short-range order of Mn^{2+} spins [17]. The magnetization sharply decreases below 80 K, which corresponds to the antiferromagnetic ordering temperature of Mn^{2+} spins (T_N). Each

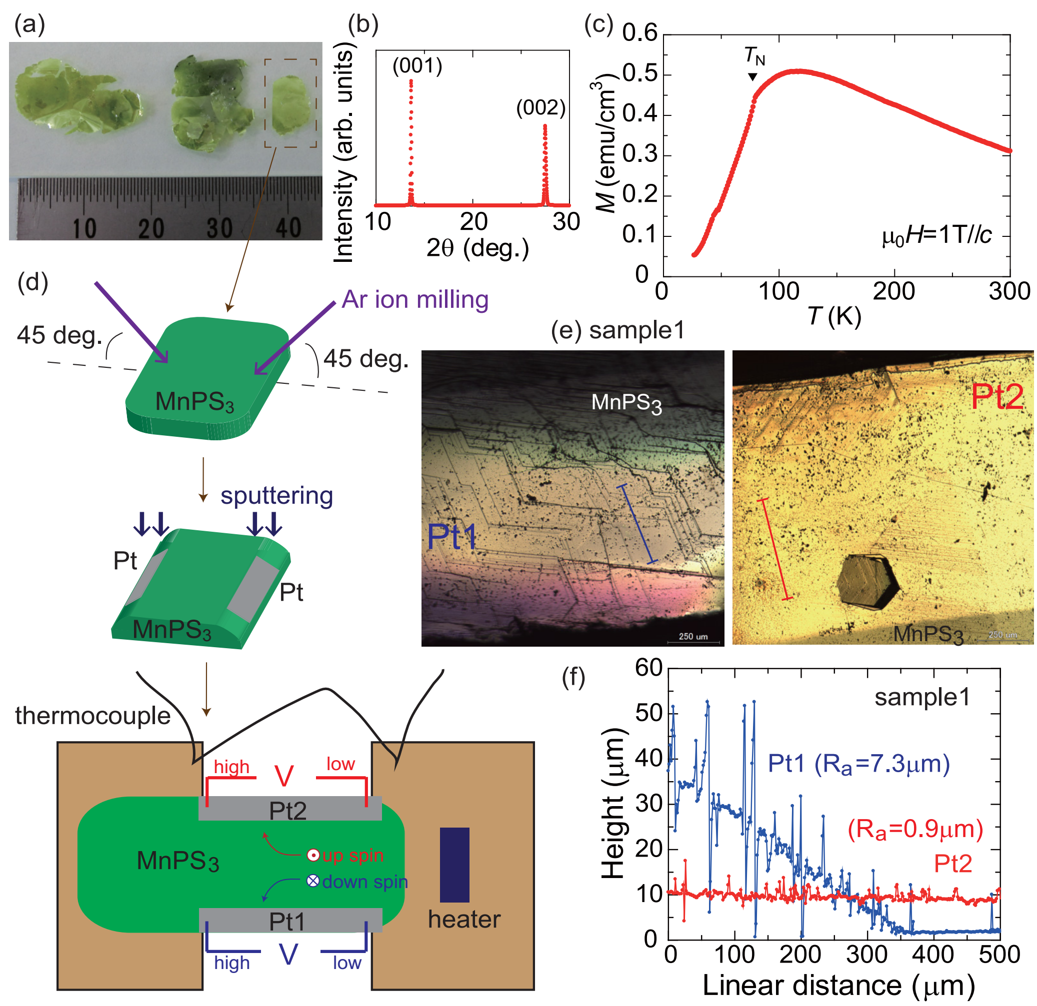

FIG. 2. (a) Examples of $MnPS_3$ single crystals. (b) X-ray diffraction pattern of a $MnPS_3$ single crystal. (c) Temperature (T) dependence of the magnetization (M) for a $MnPS_3$ single crystal. The measurement was performed under magnetic fields of 1 T applied along the c axis. (d) Flow chart of sample setup in the magnon Nernst effect measurement. After the surface treatment by Ar-ion milling processes, 5-nm-thick Pt films were deposited on the $MnPS_3$ surfaces. The Pt-$MnPS_3$ samples were fixed on two heat sinks for the measurement of thermoelectric voltages. (e) Surface images taken with a laser microscope for Pt1 and Pt2 of sample 1. (f) Distance distribution of surface heights for Pt1 and Pt2 of sample 1. This graph is obtained from the images shown in (e).

Mn^{2+} spin in the *ab* plane is coupled antiferromagnetically with the nearest neighbors and coupled ferromagnetically with the interlayer neighbors [17]. The observed *M*-*T* curve [Fig. 2(c)] is similar to that reported previously [17], which supports the high quality of our single crystals.

Seemingly homogeneous crystals of $MnPS_3$ were selected and used for the measurement of the magnon Nernst effect. Since $MnPS_3$ single crystals are soft and fragile, surface treatment by mechanical polishing is difficult, so Ar-ion milling was applied. As illustrated in Fig. 2(d), $MnPS_3$ crystals were irradiated with Ar ions at an acceleration voltage of 500 V at 45° angles to the crystal planes for 30 min on a water-cooled sample holder. The irradiation was done in the intervals of 10 min with a pause of time longer than 10 min in order to avoid damage to the sample. On both the edges of $MnPS_3$ surfaces, 5-nm-thick Pt films (with the size of $\sim 4 \times 1$ mm^2) were sputtered at room temperature in an Ar atmosphere, as shown in Fig. 2(d). Since the edges of $MnPS_3$ surfaces were made inclined naturally and/or by Ar-ion milling, the spin current flowing along a Hall direction in $MnPS_3$ can be detected using the inverse spin Hall effect in Pt.

The obtained Pt-$MnPS_3$ structures were fixed on two heat sinks using GE varnish, as shown in Fig. 2(d); on one heat sink, a 1-kΩ chip resistor was placed to generate a temperature gradient in an in-plane direction. The temperature difference between the two heat sinks, ΔT, was measured with a couple of type-E thermocouples. The thermoelectric voltage, V, measured with ϕ-25 μm Au wires for the two Pt strips (denoted by Pt1 and Pt2 hereafter) was recorded with Keithly 2182A nanovoltmeters. The measurements were performed in a cryogenic probe station in the temperature range between 10 and 200 K without external magnetic fields. Note that the values of ΔT in the thermoelectric measurements are shown in the Appendixes.

III. RESULTS

Figure 3 shows a set of experimental results for sample 1 of the Pt-$MnPS_3$ structure. In Fig. 3(a), two-wire resistivity, ρ_{Pt}^{2w}, measured between the voltage electrodes for Pt1 and Pt2, was presented. For Pt2, ρ_{Pt}^{2w} is lower than $2 \times 10^{-5}\,\Omega$ cm, which is almost the same as that of Pt films grown on an oxidized-Si substrate in our sputtering condition [18]. By contrast, ρ_{Pt}^{2w} for Pt1 is greater than 1×10^{-4} Ω cm, about ten times greater than that for Pt2. The difference in ρ_{Pt}^{2w} between Pt1 and Pt2 should be related to the roughness of the $MnPS_3$ surface, as shown in Figs. 2(e) and 2(f). The arithmetic average roughness (R_a) is 0.9 μm for Pt2-$MnPS_3$, whereas it is as large as 7.3 μm for Pt1-$MnPS_3$ in Fig. 2(e). The Pt2-$MnPS_3$ interface is much smoother than that of Pt1-$MnPS_3$; higher spin-mixing conductance is expected at the Pt2-$MnPS_3$ interface.

Figure 3(b) shows T dependence of the thermoelectric coefficients for Pt1 and Pt2 strips of sample 1, S_{Pt1} and S_{Pt2}. Here, S_{Pt1} and S_{Pt2} are defined by the thermoelectric voltage V divided by the temperature difference ΔT for Pt1 and Pt2 strips, respectively. Not only the Seebeck voltage of the Pt films but also the inverse spin Hall voltage induced by the magnon Nernst effect can contribute to S_{Pt1} and S_{Pt2} if it exists; note that the same sign of the magnon Nernst voltage is expected

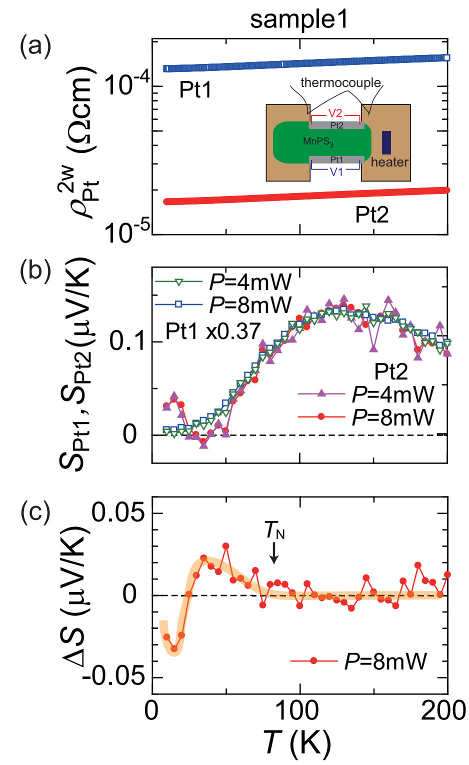

FIG. 3. Temperature (T) dependence of (a) two-wire resistivity (ρ_{Pt}^{2w}) for Pt1 and Pt2 of sample 1, (b) $V/\Delta T$ for Pt1 and Pt2 of sample 1 (S_{Pt1} and S_{Pt2}, respectively), and (c) the anomalous thermoelectric contribution defined as $\Delta S \equiv 0.37 \times S_{Pt1} - S_{Pt2}$ for sample 1. In (b), $0.37 \times S_{Pt1}$ at each T is plotted for Pt1. Here, P in (b) and (c) denotes the power level applied to the heater.

for Pt1 and Pt2 because the direction of spin polarization and also the direction of its flow are opposite between Pt1 and Pt2 [see Fig. 2(d)]. As shown in Fig. 3(b), S_{Pt1} and S_{Pt2} show a similar T dependence at high temperatures above T_N, while the magnitude of S_{Pt1} is larger than that of S_{Pt2} (see also Fig. 5). S_{Pt1} and S_{Pt2} exhibit a positive sign and show a broad peak around 120 K, which is consistent with the T dependence of the Seebeck coefficient for Pt bulk samples [19]. Hence, at high temperatures above T_N, the conventional Seebeck effect well explains S_{Pt1} and S_{Pt2}.

At low temperatures below T_N, however, S_{Pt1} and S_{Pt2} totally show different T dependencies. For high-resistance Pt1, S_{Pt1} monotonically decreases to zero as T decreases, as expected by the Seebeck effect in Pt [19]. In contrast, S_{Pt2} for low-resistance Pt2 shows a sign change from positive to negative at about 30 K, and then the sign changes again from negative to positive to exhibit a positive peak at 15 K. This highly nonmonotonic T dependence of S_{Pt2} is unlikely to be explained by the electronic origins of Pt, such as a change in dominant carriers at low temperatures, the phonon drag, or a magnetic secondary phase; such a complex electronic structure which can explain the serial sign changes (i.e., positive-negative-positive sign changes) is not observed in Pt, to the best of our knowledge. Also, the Seebeck anomaly due to the phonon drag is observed as a single peak [20]. Furthermore, impurity transport does not explain the serial

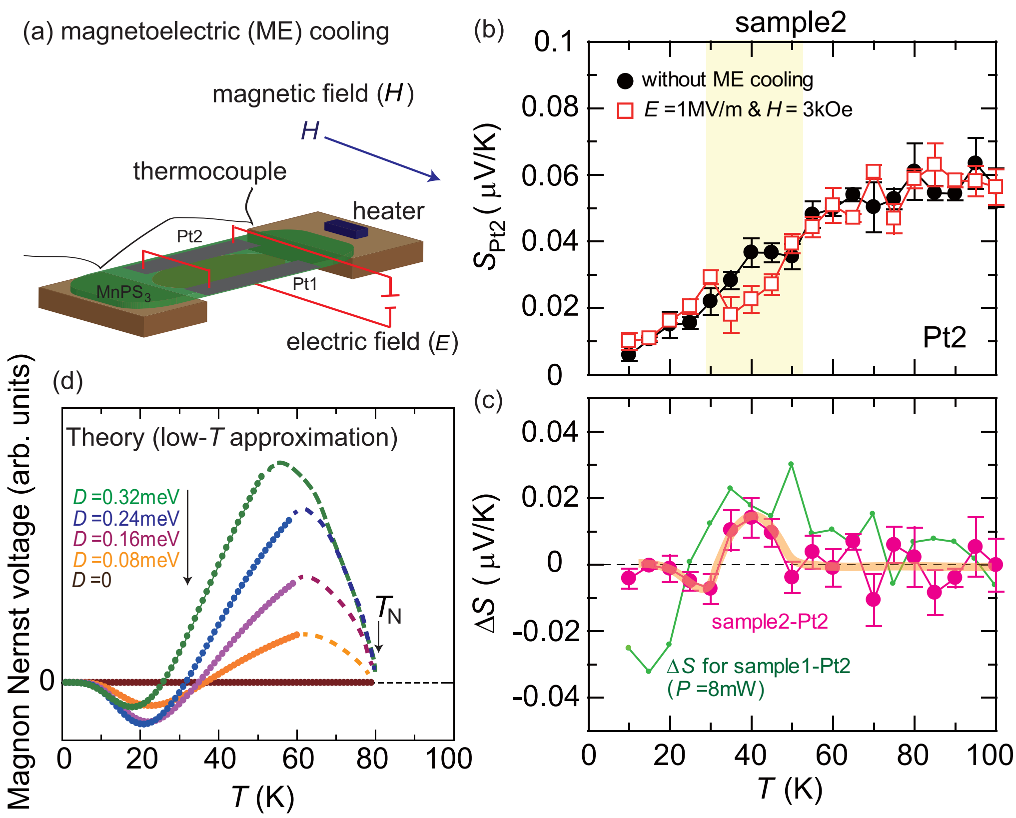

FIG. 4. (a) A schematic illustration of the experimental configuration of magnetoelectric (ME) cooling. The electric field (E) is applied along the perpendicular-to-plane direction and the magnetic field (H) is applied along an in-plane direction. (b) Temperature (T) dependence of $V/\Delta T$ for Pt2 (S_{Pt2}) of sample 2 without ME cooling (circles) and after ME cooling of $E = 1$ MV/m and $H = 3$ kOe (squares). (c) Temperature (T) dependence of the change of S_{Pt2} values by ME cooling (ΔS) for Pt2 of sample 2 (circles). The data of ΔS for Pt2 of sample 1 at $P = 8$ mW is also shown for comparison. (d) Temperature (T) dependence of the magnon Nernst signal predicted theoretically for monolayer $MnPS_3$ [10]. The calculation is only valid at low temperatures, and the magnon Nernst signal should vanish above T_N of $MnPS_3$ as indicated by dotted curves.

sign changes. Though a complicated T dependence of the Seebeck coefficient at low temperatures was reported, e.g., in Pd with dilute magnetic Ni impurities (<1 at. %) [21], Mn impurities as much as ~1 at. % in Pt films seem unlikely in our samples and the resistivity anomaly as observed in the Pd-Ni alloys [22] is not recognized in the $\rho_{\mathrm{Pt}}^{2\mathrm{w}}$-$T$ curve in Fig. 3(a). In addition, since the measurement was done in zero magnetic field, the magnetic secondary phase does not exhibit an anomalous Nernst or spin Seebeck effect. We also note that the sign changes of thermopowers in Pt may occur, owing to local variations in Seebeck coefficients due to grain boundaries and other structural features, as discussed for metal nanowires [23,24]. However, such grains and structural defects in Pt-$MnPS_3$ structures are insensitive to T, and thus it is difficult to explain the unconventional T dependence of S_{pt2} observed only in the limited T range below T_N [Fig. 3(b)]. Hence, the anomalous T dependence observed in S_{pt2} below T_N is not explained by the simple modulation of the Seebeck voltages of Pt, impurity transport, or structural defects.

Notable is that the anomalous T dependence of S_{Pt2} at low temperatures below T_N is consistent with the theoretical prediction of the magnon Nernst effect for monolayer $MnPS_3$ [10]. In Fig. 3(c), the anomalous thermoelectric contribution in S_{Pt2} is separated from the conventional Seebeck effect by plotting $\Delta S \equiv 0.37 \times S_{\mathrm{Pt1}} - S_{\mathrm{Pt2}}$. As T decreases below T_N, ΔS evolves and shows a broad positive peak around 30 K, and then sharply drops to exhibit a sign change with a negative peak at 15 K. This T dependence of ΔS is consistent with that calculated theoretically for $MnPS_3$ in Fig. 4(d), where the sign change of the magnon Nernst voltage is predicted at 20–40 K by the sign flip of the magnon Berry curvature across the von Hove singularities [10]. The sign-change temperature of about 25 K corresponds to the DM parameter (D) of ≈0.3 meV (Appendix C).

As for the indiscernible magnon Nernst voltage in the Pt1 strip of sample 1 [Figs. 3(b) and 5], several possibilities can be raised. First, the sizable roughness of $MnPS_3$ crystals as seen in Figs. 2(e) and 2(f) should decrease the spin-mixing conductance between Pt and $MnPS_3$ layers, resulting in the suppression of the magnon Nernst voltage. In our experiments, the magnitude of $\rho_{\mathrm{Pt}}^{2\mathrm{w}}$ strongly depends on the samples. It is notable that $\rho_{\mathrm{Pt}}^{2\mathrm{w}}$ for Pt2 of sample 1 is the lowest among our Pt-$MnPS_3$ samples, which indicates high spin-mixing conductance. Second, the magnon Nernst voltage is expected to be smaller than the Seebeck voltage of Pt. Large Seebeck coefficients as observed in Pt1 of sample 1 are not suitable for the detection of small magnon Nernst voltage at low

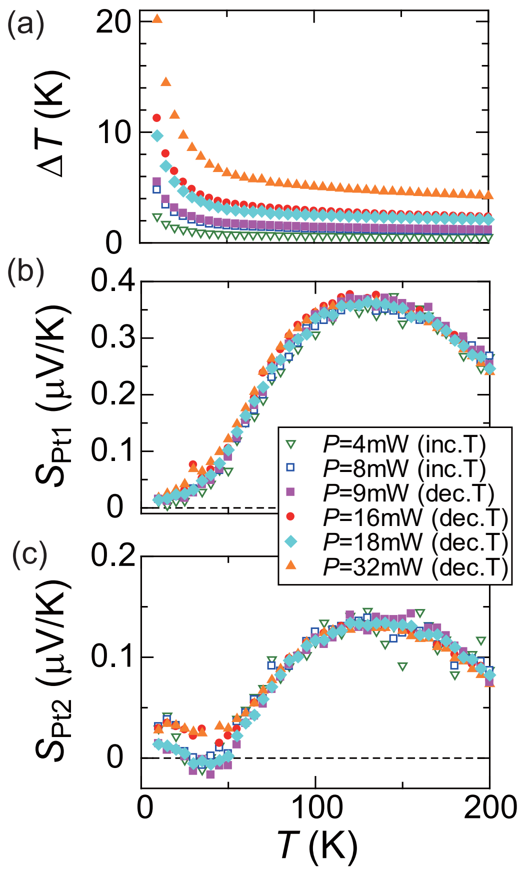

FIG. 5. Temperature (T) dependence of (a) the applied temperature difference (ΔT), (b) S_{Pt1} of sample 1, and (c) S_{Pt2} of sample 1. The experimental data at different heater power (P) levels are distinguished by means of different symbols and colors.

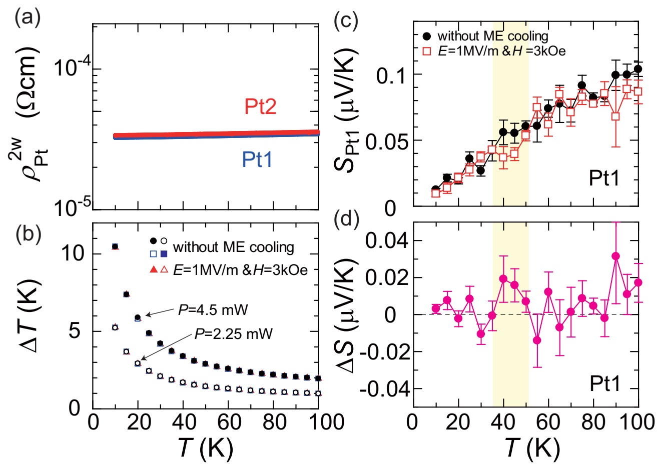

FIG. 6. Temperature (T) dependence of (a) two-wire resistivity ($\rho_{\mathrm{Pt}}^{2\mathrm{w}}$) for Pt1 and Pt2 of sample 2, (b) the applied temperature difference (ΔT) in the measurement of the magnon Nernst effect for sample 2, (c) S_{Pt1} of sample 2, and (d) the change in S_{Pt1} by ME cooling (ΔS) for sample 2. In (c) and (d), the T range where the finite ΔS signal is observed in Pt1 and Pt2 of sample 2 [Fig. 4(c)] is highlighted in yellow.

temperatures. Third, mixed antiferromagnetic domains whose boundaries disturb magnon transport can make the detection of the magnon Nernst voltage difficult.

To reveal the effect of antiferromagnetic domains in $MnPS_3$ on the magnon Nernst effect, we have investigated the dependence of the thermoelectric voltage on magnetoelectric (ME) cooling for sample 2 in Figs. 4(a)–4(c); here, $\rho_{\mathrm{Pt}}^{2\mathrm{w}}$ and the Seebeck coefficient for Pt strips of sample 2 were relatively small among our samples (Figs. 4 and 6), but the magnon Nernst voltage was not observed within our experimental accuracy. It is known that $MnPS_3$ exhibits a linear ME effect and that antiferromagnetic domains can be manipulated by cooling the sample under crossed magnetic and electric fields [25]. Although different antiferromagnetic domains are expected to produce the magnon Nernst voltage of the same sign (Appendix D), the multidomain states should reduce the magnon Nernst voltage because of disturbance of magnon transport by domain boundaries. Hence, the modulation of the thermoelectric voltage by ME cooling can corroborate the emergence of the magnon Nernst effect. As shown in Fig. 4(a), the $MnPS_3$ single crystal was subjected to electric and magnetic fields; the electric field (E) was applied along the perpendicular direction to the ab plane, while the magnetic field (H) was applied along an in-plane direction perpendicular to the Pt strips. Here, the gate-voltage electrode on the bottom surface was formed using a conductive silver paste [26], and the resistance between Pt strips and the bottom electrode was over the measurable range of multimeters. After ME cooling from 200 K down to 10 K under the simultaneous action of $E = 1$ MV/m (corresponding to 40 V) and $H = 3$ kOe, measurement of the thermoelectric voltages for Pt strips of sample was performed without any fields in increasing-T scans, as shown in Fig. 4(b). To improve the signal-to-noise ratio, the measurements were repeated three times, and the averaged data sets with error bars (meaning the standard deviation) are shown in Fig. 4(b). Obviously, the value of S_{Pt2} after the ME cooling is found to be less than that measured without the ME cooling in the T range between 30 and 50 K, while it is less sensitive to the ME cooling in other T ranges. The change in the thermoelectric voltage of Pt from the ME cooling indicates that the voltage related to the antiferromagnetic domains in $MnPS_3$ is included in the thermoelectric voltage of Pt.

The change of the S_{Pt2} values by ME cooling is calculated for Pt2 of sample 2 and is plotted against the measurement temperature, as shown in Fig. 4(c). A dome-shaped positive thermoelectric signal is tangible between 30 and 50 K. Notably, the magnitude and T dependence of the ΔS peak for sample 2 are similar to those of ΔS observed in sample 1 [Figs. 3(c) and 4(c)]. Note that, in the measurement for sample 2, the magnitudes of ΔT were set to be $\sim$10 K at 10 K (Fig. 6) to improve the signal-to-noise ratio. Hence, the low-T negative peak as observed at 15 K for Pt2 of sample 1 in Fig. 3(c) is smeared for Pt2 of sample 2 because of heating effects. The modulation of the thermoelectric voltage by ME cooling is evidence consistent with the emergence of the magnon Nernst effect for Pt-$MnPS_3$ structures. The magnitude of the inverse spin Hall voltage induced by the magnon Nernst effect is at most several tens of nanovolts in the present experiments.

IV. CONCLUSION

In summary, we measured thermoelectric voltages of Pt strips grown on the edges of $MnPS_3$ single crystals. The anomalous temperature dependence of the thermoelectric voltage for a low-resistance Pt strip on $MnPS_3$ is notably consistent with that of the magnon Nernst coefficient predicted in theoretical work [10]. Furthermore, the modulation of the low-temperature thermoelectric voltage by magnetoelectric cooling was demonstrated, which shows that the thermoelectric voltage includes spin-related voltage signals dependent on antiferromagnetic domains of $MnPS_3$. The results signal the emergence of the magnon Nernst effect in the Pt-$MnPS_3$ samples. We hope that the present work will stimulate follow-up studies on the magnon Nernst effect in antiferromagnetic insulators to harmonize the spin caloritronics, antiferromagnetic spintronics, and topological spintronics.

ACKNOWLEDGMENTS

We are grateful to S. Daimon for informing Y.S. of a theoretical paper on the magnon spin Nernst effect [10]. This work was supported by the JST ERATO Spin Quantum Rectification Project (Grant No. JPMJER1402), JSPS KAKENHI (Grants No. 17H04806, No. JP16H00977, No. 16K13827, and No. 15J01700), and MEXT (Innovative Area "Nano Spin Conversion Science" (Grant No. 26103005)).

APPENDIX A: ADDITIONAL EXPERIMENTAL DATA FOR SAMPLE 1

In Fig. 5, we show additional experimental results of the thermoelectric measurement for sample 1. Figure 5(a) shows temperature (T) dependence of the applied temperature difference, ΔT, in the thermoelectric measurement for sample 1. In the thermoelectric measurement, the heater power (P) was set to be constant at each T, and thereby the value of ΔT changes with T. The T dependence of S_{Pt1} and S_{Pt2} at $P = 4$ and 8 mW is shown in Fig. 3(b). At $P = 4$ mW, the ΔT magnitude is at most 2 K in the entire T range, and at $P = 8$ mW, at most 5 K, as shown in Fig. 5(a).

The T dependence of S_{Pt1} and S_{Pt2} at various heater power (P) levels is shown in Figs. 5(b) and 5(c), respectively. As shown in Fig. 5(b), T dependence of S_{Pt1} is almost the same among all the P values from 4 to 32 mW. By contrast, S_{Pt2} at different P values clearly shows different T dependencies in the low-T range below ∼50 K. As clearly seen in Fig. 3(b), the two sign changes are observed in the T dependence of S_{Pt2} at ∼50 K and at ∼25 K for relatively low P values. For very high P levels such as $P = 32$ mW, ΔT values reach ∼20 K at 10 K [Fig. 5(a)], and the sign changes are no longer observed in S_{Pt2} because of very strong heating effects of the sample; however, the nonmonotonic T dependence of S_{Pt2} is still observed below 50 K. Therefore, the anomaly due to the magnon Nernst effect is observed in the T dependence of S_{Pt2} at all P values. It is notable that a similar signal of the magnon Nernst effect is observed in both increasing-T and decreasing-T scans. This is consistent with the theoretical prediction that the sign of the magnon Nernst effect is the same for different antiferromagnetic domains in $MnPS_3$ (see Appendix D).

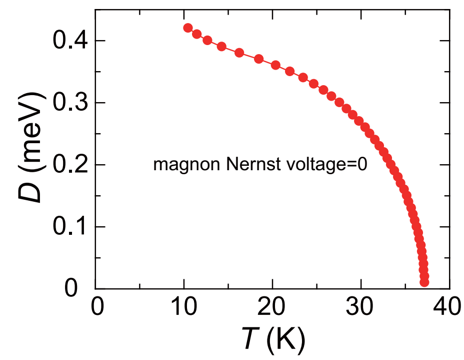

FIG. 7. The sign-change temperature of the magnon Nernst coefficient, which is calculated as a function of the Dzyaloshinskii-Moriya (DM) parameter.

APPENDIX B: ADDITIONAL EXPERIMENTAL DATA FOR SAMPLE 2

In Fig. 6, we show additional experimental results of the thermoelectric measurement for sample 2. As shown in Fig. 6(a), the magnitudes of two-wire resistivities (ρ_{Pt}^{2w}) for Pt1 and Pt2 of sample 2 are similar, and almost two times higher than ρ_{Pt}^{2w} for Pt2 of sample 1 [Fig. 3(a)].

Figure 6(b) shows the T dependence of the magnitude of ΔT in the thermoelectric measurement for sample 2. At $P = 2.25$ mW, the maximum value of ΔT is ∼5 K, whereas it is ∼10 K at $P = 4.5$ mW. The ΔT magnitudes applied for sample 2 are almost similar to those in the measurements done at $P = 8$ and 16 mW for sample 1, as shown in Fig. 5(a).

In Fig. 6(c), we show the T dependence of S_{Pt1} for sample 2. The thermoelectric measurements were performed after two different T-cooled conditions: no ME cooling [circles in Fig. 6(c)] and ME cooling [squares in Fig. 6(c)]. As shown in Fig. 6(c), a very small decrease in S_{Pt1} by ME cooling is observed for Pt1 in the T region between 30 and 50 K, similar to the change observed for Pt2 of sample 2 in Fig. 4(b).

The change in S_{Pt1} by the ME cooling (ΔS) for sample 2 is plotted in Fig. 6(d). The error level is higher for Pt1 than for Pt2, but a small positive ΔS signal is recognized for Pt1 in the T region between 30 and 50 K. In fact, the background voltage in the thermoelectric measurement was as

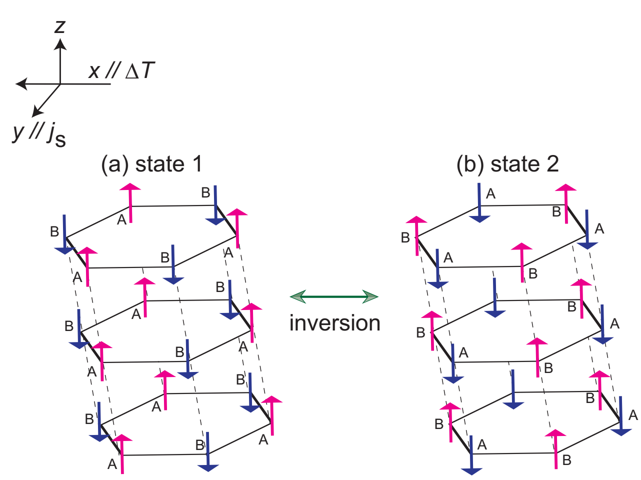

FIG. 8. Two Néel states in $MnPS_3$: (a) state 1 and (b) state 2.

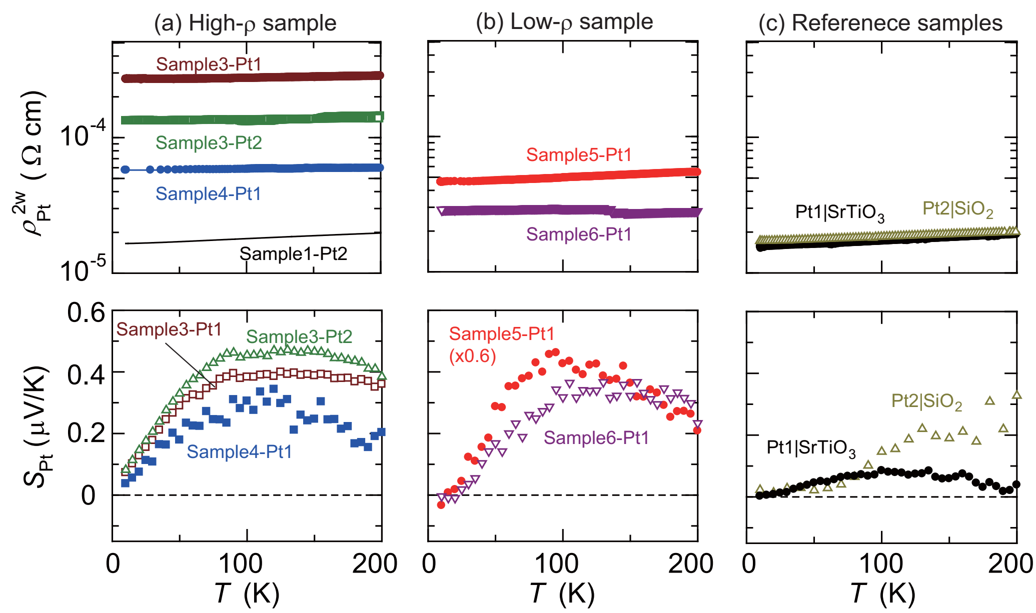

FIG. 9. Temperature (T) dependence of the two-wire resistivity (ρ^{2w}_{Pt}) and the thermoelectric coefficient (S_{Pt}) for (a) high-ρ^{2w}_{Pt} Pt-$MnPS_3$ samples ($\rho^{2w}_{Pt} \gtrsim 5\times10^{-5}\ \Omega$ cm), (b) low-ρ^{2w}_{Pt} Pt-$MnPS_3$ samples ($\rho^{2w}_{Pt} \lesssim 5\times10^{-5}\ \Omega$ cm), and (c) reference Pt samples, Pt1-$SrTiO_3$ and Pt2-SiO_2.

large as 1–1.5 μV for Pt1, while it was below 0.5 μV for Pt2; more precise measurements were thereby possible for Pt2 than for Pt1. Also, several possibilities for the tiny magnitudes of magnon Nernst voltages in some Pt-$MnPS_3$ samples, e.g., Pt1 of sample 1, are discussed in the Results section.

APPENDIX C: ESTIMATION OF THE DZYALOSHINSKII-MORIYA (DM) PARAMETER

The temperatures at which the sign of the magnon Nernst coefficient for monolayer $MnPS_3$ changes are calculated as a function of the magnitude of the DM parameter (D), as shown in Fig. 7. Here, the antiferromagnetic exchange couplings up to the third-nearest neighbors (J_1, J_2, J_3), the second-nearest-neighbor DM interaction (D), and the easy-axis anisotropy are taken into account in this calculation, as reported in [10]. As D increases, the sign-change temperature decreases [see also Fig. 4(d)]. In our experiments, the sign change of the magnon Nernst voltage is observed at 25–30 K in Figs. 3(c) and 4(c). This temperature corresponds to $D \approx 0.3$ meV.

APPENDIX D: ON THE SIGN OF THE MAGNON NERNST COEFFICIENT FOR TWO ANTIFERROMAGNETIC DOMAINS

The magnon Nernst coefficient is expected to be the same for two different antiferromagnetic domains which can coexist in $MnPS_3$ samples (Fig. 8). The magnon Nernst coefficient α^s_{xy} is defined by $\hbar(\boldsymbol{j}_\uparrow - \boldsymbol{j}_\downarrow)_y = (\partial_x T)\alpha^s_{xy}$, where $\boldsymbol{j}_{\uparrow/\downarrow}$ is the magnon current that carries ±1 spin angular momentum along the $\hat{z}$ direction. The z direction is defined as the direction perpendicular to the ab plane of $MnPS_3$.

The magnon Nernst coefficient α^s_{xy} is considered to be invariant under space inversion, since both temperature gradient and spin current are odd under the inversion of $(x,\ y,\ z) \rightarrow (-x, -y, -z)$. Furthermore, different Néel states in bulk $MnPS_3$ are connected by the inversion operation, and hence α^s_{xy} is considered to be the same for the different domains. For monolayer $MnPS_3$, similar arguments are also valid using C_2 rotation symmetry.

We can explicitly show this argument by microscopic calculations. Since the strength of the interlayer exchange coupling is two orders of magnitude smaller than that of intralayer exchange coupling [13], we here discuss the magnon Nernst effect for monolayer $MnPS_3$. As shown in [10,11], α^s_{xy} is calculated using the Berry curvature and the energy dispersion of magnons. Using the same model as studied in [10], we consider two Néel states: state 1 ($\boldsymbol{S}_{iA} = -\boldsymbol{S}_{iB} = S\hat{\boldsymbol{z}}$) and state 2 ($\boldsymbol{S}_{iA} = -\boldsymbol{S}_{iB} = -S\hat{\boldsymbol{z}}$), where $\boldsymbol{S}_{iA(B)}$ is the spin operator on the A (B) sublattices (Fig. 8). To derive the magnon modes, we first apply the Holstein-Primakoff transformation for each state:

$$S^+_{iA} \approx \sqrt{2S}a_i, \quad S^z_{iA} = S - a^\dagger_i a_i, \quad S^+_{iB} \approx \sqrt{2S}b^\dagger_i, \quad S^z_{iB} = b^\dagger_i b_i - S \quad \text{(for state 1)},$$
$$S^+_{iA} \approx \sqrt{2S}a^\dagger_i, \quad S^z_{iA} = a^\dagger_i a_i - S, \quad S^+_{iB} \approx \sqrt{2S}b_i, \quad S^z_{iB} = S - b^\dagger_i b_i \quad \text{(for state 2)}.$$

Here we emphasize that $a_i(b_i)$ carries the opposite spin angular momentum along $\hat{z}$ between states 1 and 2. The spin Hamiltonian can be expressed with these operators, and the only difference in the Hamiltonian between states 1 and 2 is

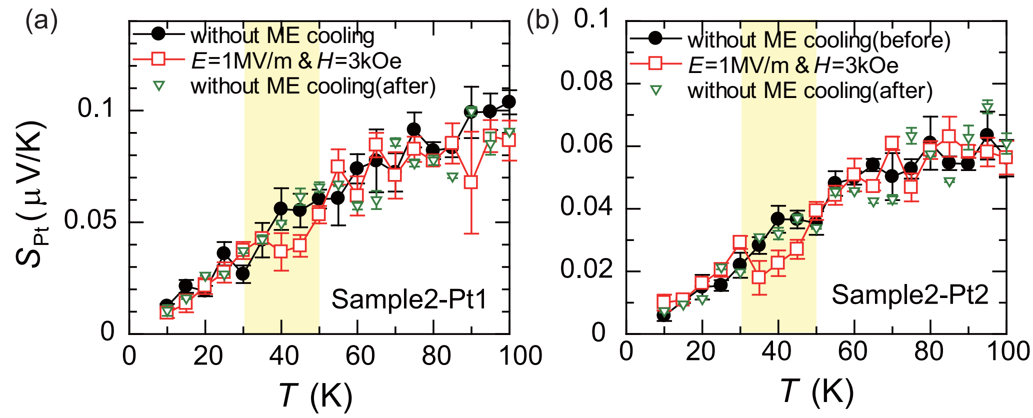

FIG. 10. Temperature (T) dependence of S_{Pt} for (a) Pt1 of sample 2 and (b) Pt2 of sample 2, measured without the ME cooling (black dots, measurement results obtained before the ME cooling experiments; green triangles, measurement results obtained after the ME cooling experiments) and with the ME cooling (red squares).

the sign of the second-nearest-neighbor DM interaction (D) given by

$$+SD\sum_{\boldsymbol{k}} g(\boldsymbol{k})(a_{\boldsymbol{k}}^\dagger a_{\boldsymbol{k}} - b_{\boldsymbol{k}}^\dagger b_{\boldsymbol{k}}) \quad \text{(for state 1)},$$

$$-SD\sum_{\boldsymbol{k}} g(\boldsymbol{k})(a_{\boldsymbol{k}}^\dagger a_{\boldsymbol{k}} - b_{\boldsymbol{k}}^\dagger b_{\boldsymbol{k}}) \quad \text{(for state 2)},$$

where $a_{\boldsymbol{k}} = \frac{1}{\sqrt{N}}\sum_i a_i e^{-i\boldsymbol{k}\cdot\boldsymbol{R}_i}$, $b_{\boldsymbol{k}} = \frac{1}{\sqrt{N}}\sum_i b_i e^{i\boldsymbol{k}\cdot\boldsymbol{R}_i}$, and $g(\boldsymbol{k}) = -g(-\boldsymbol{k})$ depends on the vectors that connect second-nearest neighbors [10].

After a Bogoliubov transformation, we obtain two magnon modes with $S^z = \pm 1$, where $S^z = \sum_i (S_{iA}^z + S_{iB}^z)$ is a good quantum number in the current system. Notably, the energy dispersions for the two modes are found to be the same between states 1 and 2 as $\hbar\omega_{\uparrow/\downarrow}^{(1)}(\boldsymbol{k}) = \hbar\omega_{\uparrow/\downarrow}^{(2)}(\boldsymbol{k})$, where $\hbar\omega_{\uparrow}^{(i)}(\boldsymbol{k})$ ($\hbar\omega_{\downarrow}^{(i)}(\boldsymbol{k})$) is the energy dispersion of the magnon with spin $S^z = +1$ (-1) for state i. The same energy dispersions for states 1 and 2 result from the fact that both the signs of the spin angular momentum along $\hat{z}$ and D are opposite between states 1 and 2. Since the Berry curvature does not depend on either D or S^z carried by each mode, the Berry curvature is also the same for states 1 and 2. Therefore, the magnon Nernst coefficient is the same for different Néel domains.

APPENDIX E: THE RELATION BETWEEN Pt RESISTIVITY AND POTENTIAL MAGNON NERNST SIGNAL

In Fig. 9, the relation between two-wire Pt resistivity ρ_{Pt}^{2w} and low-temperature thermoelectric signal S_{Pt} is investigated for various Pt-$MnPS_3$ samples. As shown in Fig. 9(a), for Pt-$MnPS_3$ samples whose ρ_{Pt}^{2w} is larger than $5 \times 10^{-5}\,\Omega$ cm, S_{Pt} has a positive sign in all the T range and monotonically decreases toward zero when $T \to 0$. In contrast, for relatively low-ρ_{Pt}^{2w} samples, where ρ_{Pt}^{2w} is almost smaller than $5 \times 10^{-5}\,\Omega$ cm (but larger than ρ_{Pt}^{2w} of Pt2 of sample 1), S_{Pt} shows a sign change from positive to negative at low temperatures, as shown in Fig. 9(b). This sign change observed for relatively low-ρ_{Pt}^{2w} samples at low temperatures may be attributed to the magnon Nernst signal, as observed in Pt2 of sample 1 (Fig. 3).

It is noted that, for a reference Pt sample grown on a diamagnetic $SrTiO_3$ substrate whose ρ_{Pt}^{2w} magnitude is comparable to that of Pt2 of sample 1 [see Fig. 9(a)], the thermoelectric coefficient is positive in the entire T regime and does not show a sign change, as shown in Fig. 9(c). The overall temperature dependence is similar to that observed in high-ρ_{Pt}^{2w} samples shown in Fig. 9(a). Also, we confirmed that the sign change is not observed in a Pt-SiO_2 sample.

APPENDIX F: DATA REPRODUCIBILITY IN THE MEASUREMENTS OF MAGNETOELECTRIC COOLING DEPENDENCE

We confirmed that, after all the measurements of the ME cooling dependence (Fig. 4), the S_{Pt} values measured without the ME cooling for sample 2 return to the original S_{Pt} values, as shown by green triangles in Fig. 10. By the ME cooling, the S_{Pt} values for sample 2 decrease in the T range between 30 and 50 K, as discussed in Fig. 4. Then, after all the measurements of the ME-cooling dependence, we again measured the T dependence of S_{Pt} without any ME cooling. As shown in Fig. 10, the obtained S_{Pt} values (green) return to the original values (black), which supports the reliability of the measurements of the ME-cooling dependence.

[1] D. Xiao, M.-C. Chang, and Q. Niu, Rev. Mod. Phys. **82**, 1959 (2010).
[2] N. Nagaosa, J. Sinova, S. Onoda, A. H. MacDonald, and N. P. Ong, Rev. Mod. Phys. **82**, 1539 (2010).
[3] J. Sinova, S. O. Valenzuela, J. Wunderlich, C. H. Back, and T. Jungwirth, Rev. Mod. Phys. **87**, 1213 (2015).
[4] H. Katsura, N. Nagaosa, and P. A. Lee, Phys. Rev. Lett. **104**, 066403 (2010).

[5] R. Matsumoto and S. Murakami, Phys. Rev. Lett. **106**, 197202 (2011).

[6] Y. Onose, T. Ideue, H. Katsura, Y. Shiomi, N. Nagaosa, and Y. Tokura, Science **329**, 297 (2010).

[7] T. Ideue, Y. Onose, H. Katsura, Y. Shiomi, S. Ishiwata, N. Nagaosa, and Y. Tokura, Phys. Rev. B **85**, 134411 (2012).

[8] M. Hirschberger, R. Chisnell, Y. S. Lee, and N. P. Ong, Phys. Rev. Lett. **115**, 106603 (2015).

[9] T. Ideue, T. Kurumaji, S. Ishiwata, and Y. Tokura, Nat. Mater. **16**, 797 (2017).

[10] R. Cheng, S. Okamoto, and D. Xiao, Phys. Rev. Lett. **117**, 217202 (2016).

[11] V. A. Zyuzin and A. A. Kovalev, Phys. Rev. Lett. **117**, 217203 (2016).

[12] O. Gomonay, T. Jungwirth, and J. Sinova, Phys. Status Solidi RRL **11**, 1700022 (2017).

[13] A. R. Wildes, B. Roessli, B. Lebech, and K. W. Godfrey, J. Phys.: Condens. Matter **10**, 6417 (1998).

[14] K. Kurosawa, S. Saito, and Y. Yamaguchi, J. Phys. Soc. Jpn. **52**, 3919 (1983).

[15] R. Brec, Solid State Ionics **22**, 3 (1986).

[16] E. Saitoh, M. Ueda, H. Miyajima, and G. Tatara, Appl. Phys. Lett. **88**, 182509 (2006).

[17] K. Okuda, K. Kurosawa, S. Saito, M. Honda, Z. Yu, and M. Date, J. Phys. Soc. Jpn. **55**, 4456 (1986).

[18] Y. Shiomi, T. Ohtani, S. Iguchi, T. Sasaki, Z. Qiu, H. Nakayama, K. Uchida, and E. Saitoh, Appl. Phys. Lett. **104**, 242406 (2014).

[19] J. P. Moore and R. S. Graves, J. Appl. Phys. **44**, 1174 (1973).

[20] R. D. Barnard, *Thermoelectricity in Metals and Alloys* (Taylor & Francis, London, 1972).

[21] C. L. Foiles, J. Phys. F: Met. Phys. **8**, 213 (1978).

[22] A. I. Schindler, and B. R. Coles, J. Appl. Phys. **39**, 956 (1968).

[23] P. Zolotavin, C. I. Evans, and D. Natelson, Nanoscale **9**, 9160 (2017).

[24] P. Zolotavin, C. Evans, and D. Natelson, J. Phys. Chem. Lett. **8**, 1739 (2017).

[25] E. Ressouche, M. Loire, V. Simonet, R. Ballou, A. Stunault, and A. Wildes, Phys. Rev. B **82**, 100408 (2010).

[26] S. Seki, Y. Yamasaki, Y. Shiomi, S. Iguchi, Y. Onose, and Y. Tokura, Phys. Rev. B **75**, 100403(R) (2007).